Freezing Vibrational Energy Flow: A Fitness Function for Interchangeable Computational and Experimental Control[†]

D. Weidinger,[§] M. F. Engel,[‡] and M. Gruebele*[,‡,§,⊥]

Departments of Chemistry and Physics, and Center for Biophysics and Computational Biology, University of Illinois, Urbana, Illinois 61801

Received: December 2, 2008; Revised Manuscript Received: January 21, 2009

We develop a fitness functional for freezing molecular energy flow that relies only on experimental observables. The functional allows us to implement a modular control algorithm where simulation data and experimental data can be used interchangeably. This interchangeability could be useful as a spectroscopic tool and for reactive control because the controllability of the experimental system and its model can be compared directly. The fitness functional performs as well as functionals based on complete knowledge of the wave function. We compare our simulation results with an analytical theory of control, and find good agreement between the simulated and predicted times over which the system can be controlled.

Introduction

A major goal of molecular spectroscopy is to extract maximum information about a molecule or reaction from the experimental data. Coherent control of molecules can be helpful in that regard, by reducing access of the system to only a part of the potentially accessible state space. Dynamics in a reduced state space could weight the experimentally accessible observables more toward the dynamics of interest.

Coherent control of molecules has been investigated extensively,[1−8] and some thought has been given to restricting dynamics in state space by coherent control.[9−12] We previously demonstrated computationally the feasibility of freezing intramolecular vibrational energy redistribution (IVR).[13] The idea is to prepare a nonstationary bright state (bright = optically accessible), followed by a shaped pulse to prevent that state from dephasing. In effect, the dipole-field coupling in the Hamiltonian offsets anharmonic vibrational couplings that ordinarily allow a bright feature in the spectrum to dephase into dark bath states. Frozen bright states are more likely than molecular eigenstates to exhibit nonstatistical couplings to the reactive continuum or to other electronic states, making them useful gateways toward understanding chemical dynamics and electronic couplings at high molecular excitation.

One shortcoming of our previous work was its use of a control functional based on knowledge of the molecular wave function. Such a control functional cannot be adapted for experimental control. This problem can be solved by a formulation in terms of observables only.[14,15] The resulting ability to substitute model and experiment for one another allows for a more direct comparison of computed and experimental control. Here we develop a control functional that is equally useful for computational and experimental implementations of freezing bright states. To that end, we rigorously separate the control algorithm into an observable module and an optimization module. Given a control field, the observable module generates experimentally measurable observables and passes only these to the optimization module. The optimization module uses only observables to compute a control functional that is used by a genetic algorithm (GA) to select an improved control field, and passes only the control field back to the observables module. No constraints (e.g., Lagrange multipliers) are involved in our optimization. Instead, a full physical model of the laser source is used.[13]

Although observables are not a perfect stand-in for complete knowledge of the wave function, a significant enhancement (up to 2 orders of magnitude in time) of the control field's ability to freeze bright states can be obtained with the best control functional we tested, using only hundreds of iterations of the GA. Our method clearly utilizes coherent control, since more trivial forms of control that rely on population cycling only, pumping isolated eigenstates, or phase-independent effects are eliminated by our laser parameters, fitness criterion, and constraints on the pulse shaper. This is a significant advantage when using fields of high intensity (10^{13} W/cm^2 or greater), as it has been demonstrated that previous experiments that control with such intense fields may not lead to the expected nonstatistical effects.[16]

The Control Model

In coherent control experiments, the control field is generated by a pulse shaper that attenuates and phase-shifts a fixed input pulse, and the system to be controlled is treated as a "black box" so that the mechanism behind the improved control is not revealed.[17−19] On the other hand, control simulations have depended on knowledge of the full wave function, and start with an arbitrary field subject to Lagrange multiplier constraints on maximum power and other parameters.[10,20−23] Bringing these two limits together imposes several requirements on the control algorithm. The control functional should depend only on observables; the shaped pulse should be physically modeled to resemble the experiment, obviating Lagrange multiplier constraints; the observables module and optimization module should pass only observables and electric fields back and forth.

We describe how a control framework that meets the above criteria may be used to freeze the dephasing of the ground-state vibrational wavepacket of a molecule. We use a sequence of three laser pulses outlined in Figure 1: an initialization pulse

---

[†] Part of the "George C. Schatz Festschrift".

* Corresponding author.

[‡] Department of Chemistry.

[§] Department of Physics.

[⊥] Center for Biophysics and Computational Biology.

10.1021/jp8106028 CCC: $40.75

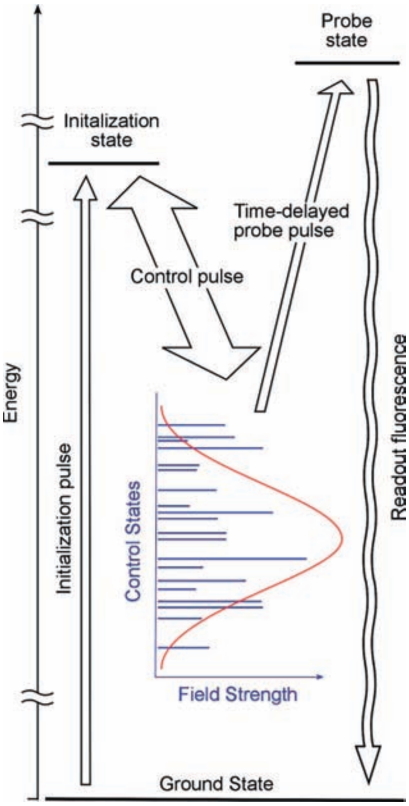

Figure 1. Schematic of the three-pulse sequence for freezing IVR and measurement. The initialization pulse pumps the molecule to an excited electronic state. The control pulse has a broad spectrum and acts to slow the dephasing of the vibrational wavepacket in the ground state. A final probe pulse pumps another electronic state after a time delay, to probe whether the ground-state wave packet remains undepahsed during control and dephases after control.

prepares the molecule in a vibrational eigenstate $|\Psi_\text{I}\rangle$ in an excited electronic state; a shaped control pulse cycles the molecule back and forth into the ground state $|\Psi_\text{C}(t)\rangle$ and controls dephasing of $|\Psi_\text{C}(t)\rangle$; finally a variable-time delay probe pulse pumps the ground-state wavepacket up to another electronic state $|\Psi_\text{P}\rangle$ from which fluorescence is measured. The latter step maps ground-state wavepacket dynamics onto a known state, providing the data needed to generate the control functional and optimize the control pulse.

Our goal is to construct a framework for interchangeable simulation-based or experiment-based freezing of a bright state $|\Psi_\text{B}\rangle$ by utilizing the same observables and control functional for both cases. The procedure is described in Figure 2; the control process is separated into an observable and an optimization module. In the observable module we list the steps for modeling the experimental output by computer simulation, but an experimental apparatus could stand in for the module as diagrammed. In the following sections, we discuss both general criteria and our specific implementation for freezing energy flow in turn.

The Target. The control target itself can be specified by a target wave function, or operationally via an experimental signal. Although we are not allowed to use knowledge of the target state in the optimization module, it is useful to define the types of target states the optimization could be asked to produce.

The prototypical goal is a bright state $|\Psi_\text{B}\rangle = \Sigma\, I_i^{1/2}|i\rangle$. In the time domain, such a bright state is nonstationary and dephases.

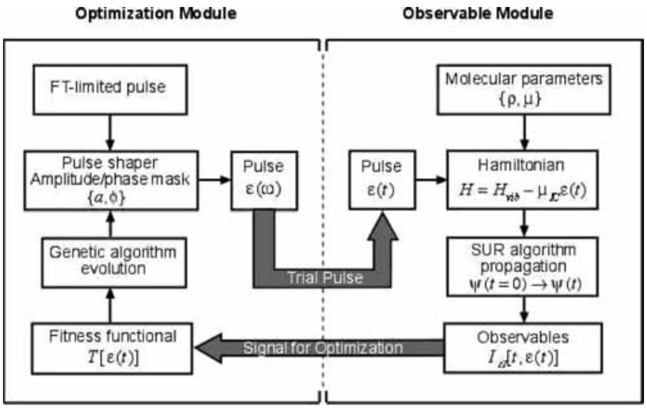

Figure 2. A flowchart of the GA pulse optimization procedure with observable and optimization modules. The observable module passes only a signal measurable by a particular experiment to the optimization module, and is thus exchangeable by an experimental output. It receives from the optimization module only information about the pulse to be tested.

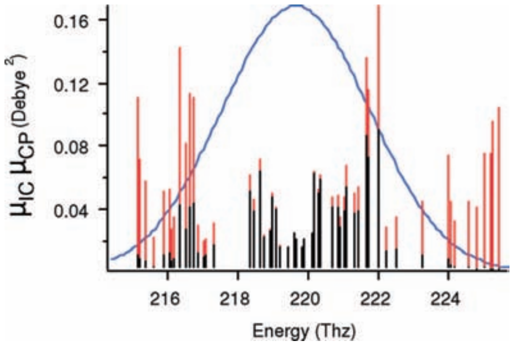

Figure 3. The spectrum of eigenstates used in the observables module, and the spectrum of the unshaped control laser pulse (smooth curve). The heights of the red bars are the $\tilde{B} \leftarrow \tilde{X}$ transition dipole moments, and the heights of the black bars are the $\tilde{A} \rightarrow \tilde{X}$ transition dipole moments.

In the frequency domain, its spectral envelope covers a clump of eigenstates with intensities I_i in the spectrum. Clumps arise because a dipole active state is anharmonically coupled to dark states, spreading its transition dipole moment over N_eff eigenstates.[24] An experimental example with intensities I_i and eigenstates $|i\rangle$ at energies E_i is shown in Figure 3 (black sticks).[25] There are $N_\text{eff} \approx 50$ eigenstates available for control.

If the control goal is to freeze the controlled state $|\Psi_\text{C}(t)\rangle$ so it equals the bright target state $|\Psi_\text{B}\rangle$ for a time t_Target, only phase pulse shaping is required. The amplitudes $|\varepsilon(\omega)|$ of the control pulse $\varepsilon(t)$ are simply held constant at values ensuring that each eigenstate $|i\rangle$ receives amplitude $I_i^{1/2}$. Of course the values assigned to $|\varepsilon(\omega)|$ need to compensate for probe transition distortion (probe field envelope and transition dipoles μ_CP are different for each eigenstate $|i\rangle$).

The task of the control field is to adjust the phases of the controlled state $|\Psi_\text{C}\rangle = \Sigma\, c_i(t)|i\rangle$ such that $c_i(t) \approx I_i^{1/2}$ as best as possible up to a maximal control time t_Target. The control field $\varepsilon(t)$ achieves control by cycling population between $|\Psi_\text{C}(t) >$ and $|\Psi_\text{I}\rangle$, attenuating undesirable parts of $|\Psi_\text{C}(t)\rangle$ by destructive interference, and building up desirable parts by constructive interference. The control field effectively cancels out the anharmonic couplings that distribute the intensity of the bright target state over the eigenstates. Ideally, this task would yield

$$
\begin{aligned}
&|\langle\Psi_B|\Psi_C(t)\rangle|^2 = 1, && 0 \leq t \leq t_{\mathrm{Target}} \\
&|\langle\Psi_B|\Psi_C(t)\rangle|^2 \approx N_{\mathrm{eff}}^{-1}, && t > t_{\mathrm{Target}}
\end{aligned}
\tag{1}
$$

Because $|\Psi_C(t)\rangle$ rapidly dephases after the control field ends, there would be a large contrast $\sim N_{\mathrm{eff}}$ between the target overlap during and after control.

We can broaden the definition of the target to include any artificially chosen envelope I_i and phase evolution. For example, we could ask that the state $|\Psi_C(t)\rangle$ produce the maximum contrast between a large probe signal during control, and no probe signal after t_{Target} has passed. In that case, amplitude pulse shaping might do better than phase-only pulse shaping: the optimal amplitude mask could enhance amplitudes near the edge of the mask to increase N_{eff}. An undesirable outcome would be for the amplitude mask to collapse $|\Psi_C(t) >$ to a single eigenstate (resulting in the desired constant probe output from $t = 0$ to $t = t_{\mathrm{Target}}$), and then to cycle that eigenstate back to the initial prepared state (mimicking the dephasing). Such outcomes would have to be designed against if a variable amplitude mask is allowed.

The fundamental problem with eq 1 is that we cannot evaluate the overlap integral experimentally. An experimentally observable replacement that guards against undesirable outcomes needs to be used in the observable module.

Observable Module. The optimization source data used here was generated by computer simulation. However, the observable module is designed to be applicable equally to closed-loop laboratory experiments.

To achieve this, the only input for the module can be a guess $\varepsilon(t)$ for the optimal control electric field, and the only output must be an experimental observable. We can broadly classify the outputs into three related groups: spectral observables, temporal observables, and averaged observables generated from either spectral or temporal observables.

Spectral observables include line positions and intensities available from continuous wave excitation. These are particularly useful for control by interference of paths through different sets of eigenstates.

Temporal observables include quantities such as absorption or fluorescence intensities as a function of pump−probe delay t_0. For a single control transition, these are fundamentally related to dipole correlation functions. For example, consider the initialization-control-probe sequence to freeze energy flow outlined in Figure 1. First a high-resolution laser prepares an initial pure quantum state $|\Psi_I\rangle$. A shaped control pulse $\varepsilon(t)$ acts on the dipole μ_{IC} to cycle population between $|\Psi_I\rangle$ and $|\Psi_C(t)\rangle$ to control $|\Psi_C(t)\rangle$. Finally a transform-limited probe pulse, centered at a variable time delay t_0 from the control pulse, projects $|\Psi_C(t)\rangle$ onto the state $\langle\Psi_P|\mu_{CP}^{\dagger}$, where $\mu_{CP}^{\dagger}$ is the transition dipole operator for the final probe step. The total fluorescence from state P varies as a function of time delay t_0 as

$$
I_{\mathrm{fl}}^{\mathrm{P}}[t_0, \varepsilon] \sim |\langle\Psi_P|\mu_{CP}^{\dagger}|\Psi_C(t_0)\rangle|^2 \tag{2}
$$

$I_{\mathrm{fl}}^{\mathrm{P}}[t_0,\varepsilon]$ can be simulated by wavepacket dynamics of $|\Psi_C(t)\rangle$, which are controlled by the field ε. Equation 2 can either be measured experimentally, or obtained by simultaneously propagating $|\Psi_I\rangle$ and $|\Psi_C(t)\rangle$ with the Hamiltonian

$$
H(t) = H_{\mathrm{vib}} - \mu_{IC}\cdot\varepsilon(t) \tag{3}
$$

TABLE 1: Frequencies (THz) and transition dipoles ($\tilde{X} \leftarrow \tilde{A}$ and $\tilde{X} \rightarrow \tilde{B}$) for the eigenstates making up the bright feature whose dephasing is to be controlled[a]

frequency (THz)	μ_{IC} (aC·pm)	μ_{CP} (aC·pm)
215.161	0.640565	6.33596
215.251	0.409841	6.33596
215.411	0.496544	4.22398
215.610	0.281133	2.98680
215.901	0.362460	5.17330
216.076	0.402642	4.72256
216.136	0.470650	2.11199
216.194	0.420496	2.98679
216.369	0.481515	10.7691
216.555	0.284579	10.5599
216.647	0.523021	7.90235
216.767	0.723985	5.57112
216.868	0.518992	2.11199
217.056	0.344642	2.11199
217.104	0.373866	2.11199
217.344	0.530424	2.11199
218.384	0.354086	6.33596
218.502	0.561199	2.98680
218.629	0.394932	6.67871
218.677	0.379440	5.17330
218.793	0.293912	2.98680
218.933	0.276019	3.65806
219.014	0.356408	5.17330
219.118	0.359134	4.22398
219.248	0.293146	2.11199
219.457	0.284052	2.11199
219.633	0.435218	2.11199
219.691	0.365139	2.11199
219.842	0.275202	2.11199
219.937	0.362253	2.11199
220.122	0.304439	2.98680
220.224	0.498202	4.72254
220.298	0.450957	4.22398
220.366	0.435565	5.17330
220.692	0.363491	4.72254
220.892	0.315804	5.58780
220.962	0.297210	4.22398
221.031	0.367797	4.72254
221.136	0.393601	6.33596
221.346	0.277644	6.67871
221.451	0.297715	6.67871
221.667	0.489548	10.1288
221.720	0.379043	11.1756
222.029	0.596060	3.87133
222.256	0.291092	1.36873
222.536	0.274110	1.76702
223.270	0.297462	2.09076
224.029	0.522878	1.93567
224.100	0.391883	1.58047
224.179	0.280331	1.58047
224.609	0.388424	1.58047
224.813	0.708280	0.79023
225.078	0.391883	2.62091
225.239	0.362460	2.84923
225.312	0.585525	2.23512
225.440	0.907552	1.58046

[a] Data derived from ref 25.

To bring the simulations as close as possible to experiment, we used experimental energies E_i to construct the vibrational Hamiltonian $E_i = \langle i|H_{\mathrm{vib}}|i\rangle$, and experimental intensities I_i to construct the transition operator $\mu_{IC} = \langle\Psi_c|\mu|i\rangle \sim I_i^{1/2}$. The actual values used here are shown in Figure 3 and Table 1. Note that eq 2 assumes a short broad bandwidth probe pulse, although a more general formula for any probe pulse is easily derived by copropagating $|\Psi_I\rangle$, $|\Psi_C(t)\rangle$, and $|\Psi_P\rangle$ instead of just $|\Psi_I\rangle$ and $|\Psi_C(t)\rangle$.

Averaged observables can be obtained from spectral or temporal observables, and are useful for imposing constraints on the optimization. An example of an averaged observable is the partially time-averaged fluorescence from state $K = I, C$, or P

$$\bar{I}_{\mathrm{K}}(t_{\min}, t_{\max}) = \int_{t_{\min}}^{t_{\max}} dt_0 I_{\mathrm{fl}}^{\mathrm{K}}[t_0, \varepsilon] \qquad (4)$$

Here $t_{\max} - t_{\min}$ is the range of time delays between control pulse and probe pulse over which the output signal is averaged. Equation 4 plays an important role in our proposed control functionals. If eq 4 is averaged long past the end of the control pulse, its value is bounded by $1/N_{\mathrm{eff}}$, the inverse number of eigenstates participating during the control process.

Optimization Module. The optimization algorithm proceeds as outlined in the left half of Figure 2. First, it obtains from the observable module the observables of the current generation $\{\varepsilon(t)\}$ of trial fields. Then the observables are used to compute the control functional for each trial field. A GA then produces a new generation of control fields based on selecting the best control functionals from the previous generation. These control fields are returned to the observable module to generate the next round of control fields. We consider each of these elements in more detail.

Most pulse shapers operate in the frequency domain, by passing pulses through a grating pair containing a discrete phase and amplitude mask. To match experiments, our optimization module operates on the control field $\varepsilon(\omega_i)$ as a function of its amplitude and phase at a set of discrete frequencies ω_i. The mask is applied to the unshaped input field $\varepsilon^{(0)}(\omega)$ (usually an unchirped csc^2 line shape of fixed intensity, often modeled by a Gaussian) according to the formula

$$\varepsilon(\omega) = \varepsilon^{(0)}(\omega) A(\omega) e^{i\varphi(\omega)} = \varepsilon_r(\omega) + i\varepsilon_i(\omega) \qquad (5)$$

The frequency domain electric field is Fourier transformed, and the time domain field $\varepsilon(t)$ for each family member of the current generation is sent to the observable module.

Each generation of trial fields is produced by a GA that attempts to increase the average control functional of successive generations of control fields. Members of the new field family that have higher control functionals than older members are allowed to enter the population, and those that have lower values are discarded.

The key to the whole procedure is a control functional that uses only experimental observables, but is robustly correlated to the desired wavepacket dynamics, in this case, freezing a bright state. Out of a large number of functionals that we tested for freezing energy flow, we determined that the best are in a class including the functional

$$T[\varepsilon(t)] = \frac{t_{\mathrm{Total}} - t_{\mathrm{Target}}}{t_{\mathrm{Target}}} \frac{\bar{I}_{\mathrm{P}}(0, t_{\mathrm{Target}})}{\bar{I}_{\mathrm{P}}(t_{\mathrm{Target}}, t_{\mathrm{Total}})} \qquad (6)$$

This functional uses averaged fluorescence from the probe state. As noted above, the control field is supposed to freeze the controlled state from 0 to t_{Target}. More fluorescence is then collected up to t_{Total}, the maximum time delay between pump and probe pulse.

The different parts of eq 6 work as follows. The constants in front ensure that the two integrals are evenly weighted, irrespective of the t_{Total} and t_{Target} chosen, although it is best to choose $t_{\mathrm{Total}} \approx 2t_{\mathrm{Target}}$.

The upper integral favors a high fluorescence signal throughout the period when IVR (dephasing) of $|\Psi_{\mathrm{C}}(t)\rangle$ is supposed to be frozen. This maximizes N_{eff} throughout the control period, avoiding solutions that briefly spike in population. The integral in the denominator makes sure that collapse of $|\Psi_{\mathrm{C}}(t)\rangle$ to a single eigenstate is not favored. Such a collapse of the wavepacket would produce large quantum beats long after the control field has switched off at $t = t_{\mathrm{targ}}$, leading to a large denominator. Instead, the ratio in eq 6 favors a large amplitude during the target time, followed by immediate dephasing of $|\Psi(t)\rangle$ after the control pulse is turned off, resulting in a small fluorescence signal $\sim 1/N_{eff}$.

When phase-only pulse shaping is used (assuming the target is $|\Psi_{\mathrm{B}}\rangle$), the underlying assumptions of eq 6 are twofold. First, that $|\langle\Psi_{\mathrm{B}}|\mu_{\mathrm{BC}}^{\dagger}|\Psi_{\mathrm{P}}\rangle| \approx \lim_{t\to\infty} N_{\mathrm{eff}} |\langle\Psi(t)|\mu_{\mathrm{BC}}^{\dagger}|\Psi_{\mathrm{P}}\rangle|$; finally, that no state other than $|\Psi_{\mathrm{B}}\rangle$ could be generated by the control field while satisfying the first assumption. These two assumptions are usually satisfied if the target and probe states are optically bright states, so their overlap with one another is large compared to their respective overlaps with the dephased state $|\Psi(t)\rangle = \Sigma\, I_i^{1/2} \exp[-iE_i t/\hbar]|i\rangle$.

The same is true when the amplitude is also shaped, although the control field can now increase the bandwidth of $|\Psi_{\mathrm{C}}(t)\rangle$ by flattening out the population distribution. With additional amplitude control, it may be necessary to take additional precautions to avoid undesirable solutions from eq 6. The control pulse could produce a $|\Psi_{\mathrm{C}}(t)\rangle$ with very few eigenstates in it, then efficiently pump them back up to $|\Psi_{\mathrm{I}}\rangle$, quenching any fluorescence from the $C \rightarrow P$ transition. This can be avoided by scaling eq 6 by $P_{\bar{\mathrm{I}}}(t_{\mathrm{Target}}, t_{\mathrm{Total}})$, putting in a penalty for strong fluorescence from the initial state, whose population should be depleted by control to produce the largest possible target amplitude.

Simulation Validation and Example. To validate eq 6 and its variants, one simply has to evaluate the overlap with the actual target state:

$$\int_0^{t_{\mathrm{Target}}} \mathrm{d}t |\langle\Psi_{\mathrm{B}}|\Psi_{\mathrm{C}}(t)\rangle|^2 \qquad (7)$$

Our specific computational implementation of the experiment outlined in Figure 1 is as follows. We use experimental molecular parameters to construct the simulation Hamiltonian eq 3. Stimulated emission pumping experiments provided the line positions and dipole magnitudes of the $\tilde{A} \rightarrow \tilde{X}$ transitions of thiophosgene listed in Table 1. The simulations reported in this paper presume an initial population prepared entirely in the $|\Psi_{\mathrm{I}}\rangle = |101100\rangle$ vibrational state of the $\tilde{A}$ electronic state, 19673 cm^{-1} above the ground-state origin. The control field $\varepsilon(t)$ creates a nonstationary state $|\Psi_{\mathrm{C}}(t)\rangle$, whose dephasing is to be frozen on the $\tilde{X}$ state electronic surface. We simulated a mask with up to 128 amplitude and phase control parameters. The input field $\varepsilon^{(0)}$ corresponds to a transform-limited regeneratively amplified Ti:Sapphire laser output: 1 mJ maximum energy per pulse, and a bandwidth of 8 THz at 810 nm. Time propagation of eq 3 is accomplished by the SUR propagator.[26,27]

The observable module is not allowed to pass $|\Psi_{\mathrm{C}}(t)\rangle$ to the optimization module, only quantities of the type illustrated in eq 2. $\langle\Psi_{\mathrm{P}}|\mu_{\mathrm{CP}}^{\dagger} = \langle 000000|\mu_{\mathrm{XB}}^{\dagger}$ in this case was given by the ground vibrational state of the $\tilde{B}$ electronic state, and μ_{CP} was the $\tilde{B} \leftarrow \tilde{X}$ transition dipole magnitude, also listed in Table 1. The resulting observable can be measured experimentally by delaying the $\tilde{B} \leftarrow \tilde{X}$ probe pulse with respect to the $\tilde{A} \leftrightarrow \tilde{X}$ control pulse, and plotting the total fluorescence from the $\tilde{B}$ state as a function of the time delay. (We use the double arrow for the control pulse because it cycles significant population both ways.)

Equation 6 could thus be evaluated experimentally, or by the observable module. To set up the control functional, we found that $t_{\text{tot}} \geq 2t_{\text{Target}}$ provides a satisfactory result. In our simulations, we chose $t_{\text{Target}} \approx 7.7$ ps near the maximum achievable with our input pulse bandwidth of 30 THz in a 128 pixel pulse shaper. The GA[28] creates new generations using mutation or crossover (the swapping of parameters).

To speed the convergence of the GA, the phase and amplitude control parameters $\varphi(\omega_i)$ and $A(\omega_i)$ are represented in a Haar wavelet basis, as in our past work. This allows the GA to operate at independent resolution levels from the individual pixel to the entire pulse shaper and quickly find solutions for large portions of frequency space that have a simple optimum state (e.g., completely attenuated). The resolution level is incremented as the fitness at each order of resolution converges. The process continues until single-pixel resolution is attained.

Several modifications of the basic GA were necessary for the wavelet coefficients to transform and converge properly. When incrementing the wavelet resolution, newly available coefficients should be set to nonzero values or genetic diversity will suffer. We perform this transform, σ_i, in the pixel basis and increment the coefficients by an amount randomly chosen within the range that observes the boundary conditions. The full transform is

$$\begin{bmatrix} w_{0,0} \\ w_{1,0} \\ w_{2,0} \\ w_{2,1} \\ 0 \\ 0 \\ 0 \\ 0 \end{bmatrix} \xrightarrow{\text{IWT}} \begin{bmatrix} a_0 \\ a_0 \\ a_1 \\ a_1 \\ a_2 \\ a_2 \\ a_3 \\ a_3 \end{bmatrix} \xrightarrow{\sigma_i} \begin{bmatrix} a_0 + rand(\sigma_0) \\ a_0 - rand(\sigma_0) \\ a_1 + rand(\sigma_1) \\ a_1 - rand(\sigma_1) \\ a_2 + rand(\sigma_2) \\ a_2 - rand(\sigma_2) \\ a_3 + rand(\sigma_3) \\ a_3 - rand(\sigma_3) \end{bmatrix} \xrightarrow{\text{WT}} \begin{bmatrix} w_{0,0} \\ w_{1,0} \\ w_{2,0} \\ w_{2,1} \\ w_{3,0} \\ w_{3,1} \\ w_{3,2} \\ w_{3,3} \end{bmatrix} \qquad (8)$$

where IWT and WT are the inverse and regular Haar wavelet transforms. Mutation is accomplished in a similar manner; the wavelet coefficient selected for mutation is only allowed to vary within limits set in the pixel basis.

Genetic crossover may simultaneously adjust many wavelet coefficients, so boundary conditions are met by transforming altered vectors into the pixel basis and truncating values that exceed bounds. We tested several methods of crossover and found that using a modified two-point crossover technique provided the best solutions. In two-point crossover, two vectors exchange portions of arbitrary length; our program selects one point in the wavelet vector to begin exchanging and switches all subsequent coefficients of the same resolution level. This method produces vectors with an average fitness a factor of 2 higher than one-point crossover, which exchanges all coefficients from the starting point to the end of the vector.

Results

Figure 4 shows the freezing achieved in a typical amplitude + phase control simulation. The unshaped pulse produces a rapid decay of probe fluorescence, followed by a small baseline $\approx N_{\text{eff}}^{-1}$ after the peak. The controlled amplitude is not smooth, but produces greatly enhanced fluorescence over the 7.7 ps control period compared to the unshaped pulse. Analysis of the wavepacket shows that there are two very different reasons for the large contrast of signal during and after control. One is that the control amplitude enhances transitions in the wings compared to the center frequency, increasing N_{eff}. The other reason is back-pumping of the controlled wavepacket to the initial state when the control period is over. This is not necessarily detrimental to control. The overlap of controlled state and the bright target state of Figure 3/Table 1 is substantial (black trace). As long as the controlled state does not have a collapsed bandwidth, back-pumping actually can be beneficial: it removes the freely evolving wavepacket after the control period is over, preventing any dephased population from reacting or undergoing other postcontrol dynamics.

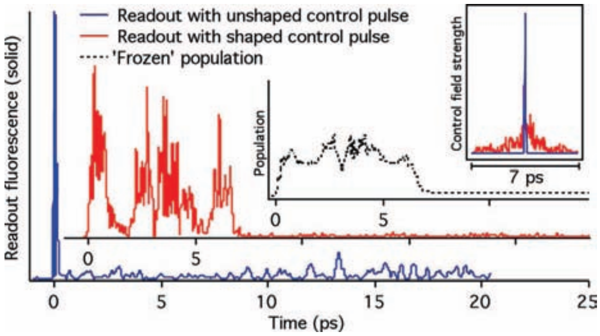

Figure 4. Optimized amplitude and phase freezing of IVR involving the states in Figure 3. Bottom (blue) curve: fluorescence probe signal from the $\tilde{B}$ state of thiophosgene for the unshaped control pulse in Figure 3; middle (red) curve: same signal for the pulse optimized to freeze IVR for 7 ps; top (black) curve: total population in the control states weighted by the square of the $\tilde{B}$ state transition dipole moments. Inset: intensities of the unshaped (blue) and shaped (red) control pulses.

Figure 5 shows a more detailed characterization of the control process. The full wavelet hierarchy was used to achieve control, although the windowed Fourier transform of the control pulse shows a relatively simple structure with alternating down and up frequency chirps. The phase structure of the pulse is more complex than its amplitude structure, which could be further economized by not varying amplitude in spectral regions of low line density. To some extent, such varying-resolution control is achieved by the wavelet representation.

Given the ca. 50 eigenstates involved in the control, one would expect to need the full resolution of the pulse shaper, especially because the eigenstates in Figure 3 are not evenly spaced. Figure 6 proves this indeed to be the case. The fitness of the control field decreases by about a factor of 2 for every factor of 2 in resolution. Reoptimizing at a given resolution level slightly improves performance, but not back to the full level.

The comparison of amplitude + phase control in Figures 4 and 7 with phase-only control in Figure 8 (the red traces) shows that a similar extent of control and population transfer can be achieved with just the phase. The phase-only control produces good overlap with its target state. Indeed, the fluorescence trace in Figure 8 is very close to the target overlap in Figure 8, showing that the functional in eq 6 is an excellent substitute for the actual target overlap during phase-only control. This results because the amplitudes are already constrained to the desired bright state, and $|\Psi_{\text{P}}\rangle$ is a good stand-in for $|\Psi_{\text{B}}\rangle$ when it comes to just preventing dephasing.

Both in figure 4 and in figure 7, amplitude control using eq 6 appears to be better than phase-only control at suppressing recurrences after t_{Target}, leading to a very large apparent $N_{\text{eff}} >$

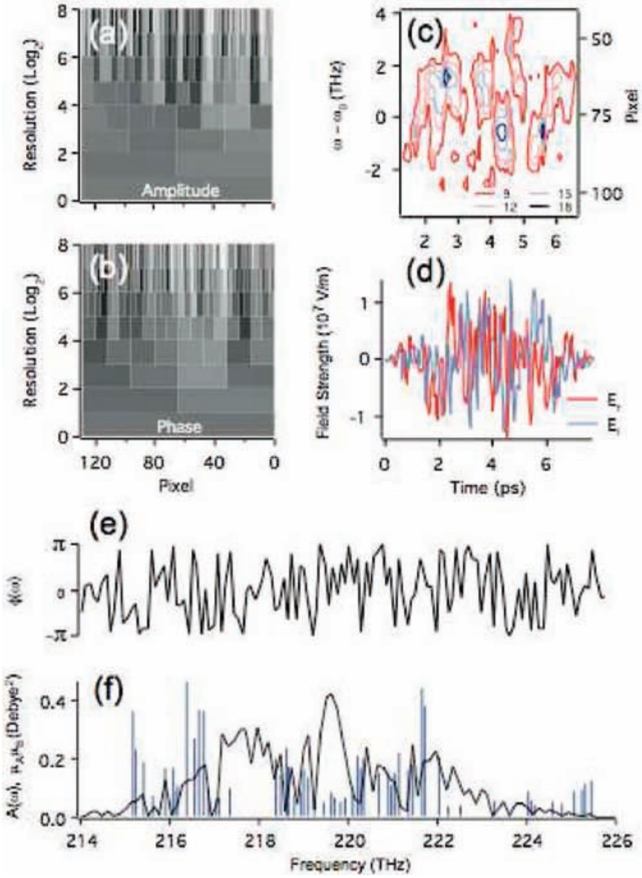

Figure 5. A plot of the amplitude (a) and phase (b) masks for one optimized control pulse. In each graph, the lowest row represents the pixel values at the lowest resolution of the wavelet basis, and each row increments the resolution by a factor of 2 up to the full 128 pixel representation. (Pixel values are white for full amplitude or phase shift of π and black for zero amplitude or a phase shift of $-\pi$.) Panel c is a vibrogram of the pulse and panel d shows the real (red) and imaginary (blue) parts of the electric field in time. Panel e is the phase mask in the frequency domain, and panel f shows the magnitude of the field in the frequency domain along with the product of the $\tilde{B} \leftarrow \tilde{X}$ and $\tilde{A} \rightarrow \tilde{X}$ transition dipole moments from Figure 3.

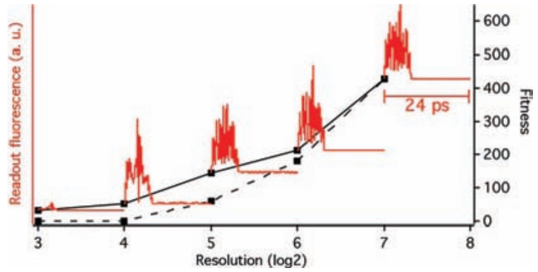

Figure 6. A set of fitnesses at shaper mask resolutions from 2^3 to 2^7 pixels. The dashed line uses the low resolution components of the maximum resolution mask. The solid line was reoptimized at each resolution level. Traces of 24 ps of fluorescence yield (red) corresponding to each mask are attached to each point.

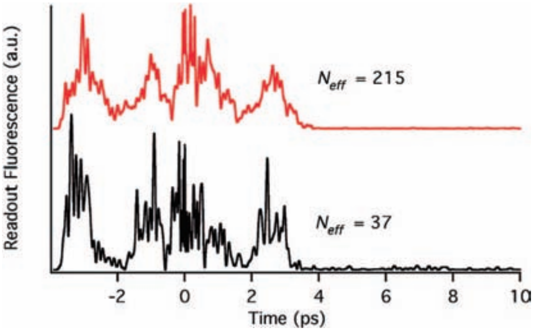

Figure 7. Readout fluorescence for a $t_{\mathrm{Target}} = 7$ ps optimization with amplitude + phase mask. Top (red): using the functional in eq 6; bottom (black): using the amended fitness functional described in eq 10. Equation 6 only finds pulses that removed population from the dipole-active states when control is over and eliminates fluorescence after t_{Target}. This condition improved the fitness by a factor of 10, as evidenced by the large apparent value value for N_{eff}. The amended eq 6 does not pump population back, so quantum beats in the dephased population can be observed.

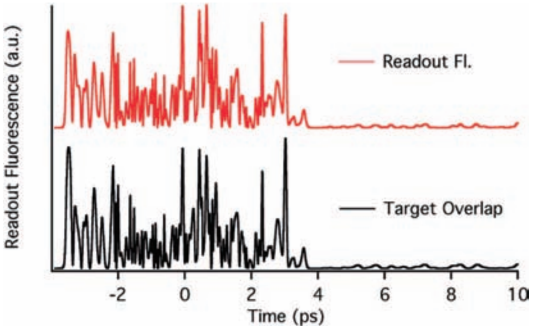

Figure 8. A $t_{\mathrm{Target}} = 7$ ps optimization with phase mask only. Top (red): readout fluorescence using eq 6. Bottom (black): overlap with the bright state with eigenstate amplitudes given by $c_i = \varepsilon_{\mathrm{C}}^{(0)}(\omega_i)\varepsilon_{\mathrm{P}}(\omega_i)\mu_{\mathrm{IC}}\mu_{\mathrm{CP}}$ (the product of the $\tilde{A} \rightarrow \tilde{X}$ and $\tilde{B} \leftarrow \tilde{X}$ spectra in Figure 3).

200 in Figure 7. Such a large contrast of fluorescence intensity during control and after control cannot be achieved with only ca. 50 eigenstates in the bright state. Figure 7 investigates further the cause of this large contrast: how much is due to amplitude shaping broadening of the bandwidth and increasing N_{eff}, and how much is due to the amplitude-shaped pulse cycling population back to the initial state more efficiently, suppressing the probe transition after control is over? The bottom of Figure 7 shows the effect of including a penalty in eq 6 for initial state ($|\Psi_{\mathrm{I}}\rangle = \tilde{A}$ state) fluorescence. This reduces the amount of population pumped back to the initial state at the end of the amplitude + phase control period. The contrast between controlled and free probe fluorescence is now just slightly larger than in the phase-only case, with $N_{\mathrm{eff}} \approx 40$ in both cases. This shows that the large contrast achieved with amplitude + phase is mainly due to better recycling of the control population after control is over.

There is one more way in which amplitude shaping can decrease the baseline signal at $t > t_{\mathrm{Target}}$. As can be seen in Figure 3, the $\tilde{A} \leftrightarrow \tilde{X}$ control transition and $\tilde{B} \leftarrow \tilde{X}$ probe transition do not access the same set of vibrational levels in the ground electronic state. By "parking" population in states inaccessible by the probe transition, the control pulse can feign a low population in the controlled wavepacket after control has elapsed. Indeed, the amplitude + phase control without additional constraints in Figure 7 parks about twice as much population in eigenstates with low transition dipoles from $\tilde{B} \leftarrow \tilde{X}$ than similar phase-only control in Figure 8, whose fixed target amplitude $c_i = \varepsilon_{\mathrm{C}}^{(0)}(\omega_i)\varepsilon_{\mathrm{P}}(\omega_i)\mu_{\mathrm{IC}}\mu_{\mathrm{CP}}$ excludes such states from being populated.

Finally, one might ask whether the multiple solutions of the control field found here are in the same optimized basin. If so, averaging several solutions together in either the time domain or in the frequency domain would also yield good control. This is not the case. The illustrated average of 10 optimized solutions in Figure 9 produces a fluorescence signal with no contrast

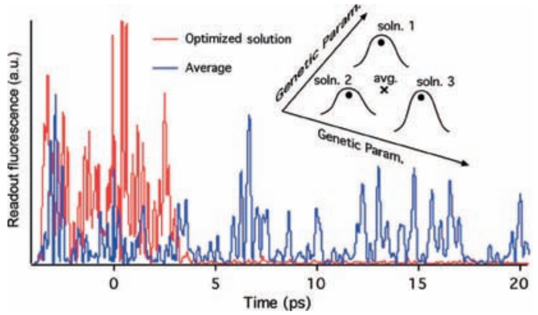

Figure 9. Probe fluorescence from the $\tilde{B}$ state of thiophosgene, for the most fit pulse after GA optimization (red), and for the average of 10 similarly optimized pulses (blue), each beginning with different randomly chosen input parameters. The average does not provide any control of IVR.

between the control period and free evolution period. A large number of equally good but distinct solutions to the control problem exists.

Discussion

For a pulse shaper covering 8 THz of bandwidth with 128 pixel resolution, the expected maximum control duration (Nyquist limit) is about 8 ps, and we are clearly able to achieve freezing of IVR over this time scale with a fitness functional using only experimentally available data. The key to making a functional not based directly on the vibrational wavepacket work is the nature of the IVR process: the initial, target, and probe states have simple nodal structures and hence strong Franck−Condon overlaps, while the dephased state to be avoided has low overlap with these three states. This "negative design" approach, avoiding the undesirable outcome rather than designing for the desired outcome, allows eq 6 to differentiate the target from the dephased state that results from the unassisted vibrational dynamics of the molecule.

One consequence of this difference between bright and dephased states is the ability of amplitude + phase control to find reasonable solutions, i.e., solutions whose fluorescence contrast does not just arise from back-pumping of the population to the initial state or parking it in states hidden from the probe transition. For simulations that maintained a large population in the control state, the addition of amplitude shaping did not enhance the fitnesses further by more than a factor of 2 (bottom of Figure 7 compared to the top of Figure 8). If one wishes to freeze a specific bright state, rather than to obtain the fastest dephasing after the control pulse ends, the additional bandwidth of the vibrational wavepacket created by amplitude shaping is not necessary, and one can simply do phase-only pulse shaping. The amplitudes are then fixed at the desired target amplitude, and the control field only prevents dephasing of the eigenstates making up the bright target state.

Rabitz and co-workers have discussed that coherent optimal control generally allows for many near-optimal solutions, that is, the control landscape is rugged.[29] This notion is confirmed by our application, as Figure 9 clearly shows that, while multiple solutions can be found, averages of these solutions provide little or no control. The solutions are dissimilar in that sense. This has been considered a disadvantage (lack of robustness), but it actually provides robustness against variation of external parameters beyond the control of the experimenter. In the presence of additional external constraints, it is more likely that one can still find a viable solution among the less constrained solution set. A typical example of such an external parameter is the laser fluence seen by the molecule. Control experiments typically used focused laser pulses that have not been shaped spatially to provide uniform power, so different molecules see the same temporal field, but with different fluences. We recently showed that, for a quantum computing control problem, many solutions can be found, but that when solutions are asked to work optimally at many laser powers, a subset of these solutions still performs well.[8]

It would be interesting to see how close to the limit of controllability the 8 ps control in Figure 4 comes. The quantized version of Ulam's conjecture on transport in weakly chaotic classical systems provides a quantitative prediction for controllability.[30] The idea of the quantized Ulam conjecture is to connect the initial and target states as efficiently as possible as allowed by anharmonic couplings and transition dipoles, and to set bounds on the time and laser fluence required, assuming the field can be shaped arbitrarily subject to these two constraints. The limit on controllability is given by

$$t_{\mathrm{Target}} \geq \frac{N_{\mathrm{tot}}}{N_{\mathrm{loc}}} \frac{2h^2 c\varepsilon_0}{\mu_0{}^2 f} \qquad (9)$$

In this equation, t_{Target} has already been defined, f is the laser fluence (in W/m^2), c is the speed of light, ε_0 is the dielectric constant of the vacuum, and μ_0 is the transition dipole moment coupling the initial and bright state. The ratio $N_{\mathrm{tot}}/N_{\mathrm{loc}}$ is a measure of how strongly chaotic the system is; N_{tot} is the total number of states within the control bandwidth, while N_{loc} is the local number of states coupled directly to the target bright state; the limit of classical chaos corresponds to $N_{\mathrm{tot}}/N_{\mathrm{loc}} \rightarrow 1$ quantum-mechanically. For $SCCl_2$ at the conditions shown in Figure 3 and Table 1, the parameters are $N_{\mathrm{tot}} = 5700$, $N_{\mathrm{loc}} = 20$, $\mu_0 = 8 \times 10^{-31}$ Cm, and $f = 25\,000$ J/m^2 (mJ pulse and 200 μm focus), which sets $t_{\mathrm{Target}} \geq 2$ ps. Thus the model of controllability predicts the minimal control time and indeed, we obtained best results controlling over 7.7 ps, a time approaching the bandwidth limit of our pulse shaper model.

Before settling on eq 6 and its fluorescence-weighted variants, we tested a large number of control functionals. For example, since the ideal $T[\varepsilon(t)]$ would be a constant up to t_{Target}, then drop to $1/N_{\mathrm{eff}}$ thereafter, we tested functionals that minimize the variance of the fluorescence signal during the control period. These and other functional forms did not perform as well as eq 6. The only comparable performance we observed was by using functionals that had direct access to the phases and amplitudes of the eigenstates making up $|\Psi_C(t)\rangle$, but this type of information is of course not accessible experimentally. The functional in eq 6 performed essentially as well as the direct overlap $|\langle\Psi_B|\Psi_C(t)\rangle|^2$, as can be seen by comparing the corresponding traces in Figure 4, and especially in Figure 8 (phase-only control).

As described above, it may be useful during amplitude pulse shaping to design against "parking" population in states inaccessible to the probe pulse. A possible modification to eq 6 is to multiply the fitness functional by the term

$$\left(1 + \frac{S}{S_{\max}}\right), \quad \text{where} \quad S = \sum_i |c_i(t_{\mathrm{Target}})|^2 |\mu_{\mathrm{CP},i}|^2 \qquad (10)$$

S is the dipole-weighted population in the control state at t_{Target}, and $S_{\max}$ is its maximum possible value. In the simulations, this quantity was computed directly from the control wave function coefficients. In an experiment, it could be measured by collecting the total fluorescence from the probe state after it has been populated by a pulse at t_{Target}. This modification is useful because it favors solutions that maintain a large population in only those energy levels of $|\Psi_C(t)\rangle$ that couple strongly to the probe state $|\Psi_P\rangle$. Equation 6 by itself favors no particular eigenstate in $|\Psi_C(t)\rangle$, which would be a problem if an eigenstate $|i\rangle$ is accessed by the $I \rightarrow C$ transition moment, but not by the $C \rightarrow P$ transition moment, preventing it from contributing to the fitness functional. Inclusion of eq 10 in the control functional suppressed the parking of population in dark states by a factor of 2.

To conclude, phase-only control with a control functional based on measurable pump–probe fluorescence freezes IVR essentially as well as wave function-based functionals we tested previously. Amplitude control is also possible, but requires additional precautions to avoid populations inaccessible to the probe transition, while back-pumping of the wavepacket after control is over can be beneficial because a dephasing population is avoided. The modular observable/optimization approach allows direct substitution of experimental or simulated data, which should allow a better comparison of the controllability of experimental and simulated systems. The latter can then be used to gain insight into the origin of controllability in the experiment. For freezing IVR, our results are in agreement with a general model of controllability of quantum systems that are analogous to weakly chaotic classical systems, the quantized Ulam conjecture.

Acknowledgment. Computations were performed on a cluster funded by NSF CRIF CHE-0541659. This work was supported by a James R. Eiszner Professorship, and by the Research Board of the University of Illinois (Grant RB 05255).

References and Notes

(1) Rabitz, H.; Vivie-Riedle, R. d.; Motzkus, M.; Kompa, K. *Science* **2000**, *288*, 824.

(2) Herek, J. L.; Wohlleben, W.; Cogdell, R. J.; Zeidler, D.; Motzkus, M. *Nature* **2002**, *417*, 533.

(3) Levis, R. J.; Rabitz, H. A. *J. Phys. Chem. A* **2002**, *106*, 6427.

(4) Pegarkov, A. I. *J. Chem. Phys.* **2005**, *123*, 104313.

(5) Hauer, J.; Skenderovic, H.; Kompa, K. L.; Motzkus, M. *Chem. Phys. Lett.* **2006**, *421*, 523.

(6) Bergt, M.; Brixner, T.; Kiefer, B.; Strehle, M.; Gerber, G. *J. Phys. Chem. A* **1999**, *103*, 10381.

(7) Zhao, M. Y.; Babikov, D. *J. Chem. Phys.* **2007**, *126*, 204102.

(8) Weidinger, D.; Gruebele, M. *Mol. Phys.* **2007**, *105*, 1999.

(9) Gruebele, M.; Bigwood, R. *Int. Rev. Phys. Chem.* **1998**, *17*, 91.

(10) Ohtsuki, Y.; Nakagami, K.; Fujimura, Y.; Zhu, W. S.; Rabitz, H. *J. Chem. Phys.* **2001**, *114*, 8867.

(11) Gruebele, M. *J. Phys.: Condens. Matter* **2004**, *16*, R1057.

(12) Dian, B. C.; Longarte, A.; Winter, P. R.; Zwier, T. S. *J. Chem. Phys.* **2004**, *120*, 133.

(13) Bigwood, R. M.; Gruebele, M. *J. Mol. Struct. (THEOCHEM)* **2002**, *589*, 447.

(14) Mitra, A.; Rabitz, H. *J. Chem. Phys.* **2008**, *120*, 044112.

(15) Sharp, R.; Mitra, A.; Rabitz, H. *J. Math. Chem.* **2008**, *44*, 142.

(16) Lozovoy, V. V.; Zhu, X.; Gunaratne, T. C.; Harris, D. A.; Shane, J. C.; Dantus, M. *J. Phys. Chem.* **2007**, *112*, 3789.

(17) Bardeen, C. J.; Yakovlev, V. V.; Wilson, K. R.; Carpenter, S. D.; Weber, P. M.; Warren, W. S. *Chem. Phys. Lett.* **1997**, *280*, 151.

(18) Assion, A.; Baumert, T.; Bergt, M.; Brixner, T.; Kiefer, B.; Seyfried, V.; Strehle, M.; Gerber, G. *Science* **1998**, *282*, 919.

(19) Hornung, T.; Meier, R.; Motzkus, M. *Chem. Phys. Lett.* **2000**, *326*, 445.

(20) Peirce, A. P.; Dahleh, M. A.; Rabitz, H. *Phys. Rev. A* **1988**, *37*, 4950.

(21) Hornung, T.; Motzkus, M.; de Vivie-Riedle, R. *Phys. Rev. A* **2002**, *65*, 021403.

(22) Zhu, W. S.; Rabitz, H. *J. Chem. Phys.* **2003**, *118*, 6751.

(23) Werschnik, J.; Gross, E. K. U. *J. Phys. B: At., Mol. Opt. Phys.* **2007**, *40*, R175.

(24) Nesbitt, D. J.; Field, R. W. *J. Phys. Chem.* **1996**, *100*, 12735.

(25) Strickler, B.; Gruebele, M. *Phys. Chem. Chem. Phys.* **2004**, *6*, 3786.

(26) Bigwood, R.; Gruebele, M. *Chem. Phys. Lett.* **1995**, *233*, 383.

(27) Engel, M.; Gruebele, M. *Chem. Phys. Lett.* **2007**, *433*, 368.

(28) Charbonneau, P. *Astrophys. J. Supplement Series* **1995**, *101*, 309.

(29) Shir, O. M.; Beltrani, V.; Back, T.; Rabitz, H.; Vrakking, M. J. J. *J. Phys. B: At., Mol. Opt. Phys.* **2008**, *41*, 074021.

(30) Gruebele, M.; Wolynes, P. G. *Phys. Rev. Lett.* **2007**, *99*, 060201.

JP8106028